09/17/2014 Revision

Tissintite, $(Ca,Na,\square)AlSi_2O_6$, a highly-defective, shock-induced, high-pressure clinopyroxene in the Tissint martian meteorite

Chi Ma[a,*], Oliver Tschauner[b], John R. Beckett[a], Yang Liu[c], George R. Rossman[a], Kirill Zuravlev[d], Vitali Prakapenka[d], Przemyslaw Dera[e], Lawrence A. Taylor[f]

[a] Division of Geological and Planetary Sciences, California Institute of Technology, Pasadena, California 91125, USA

[b] High Pressure Science and Engineering Center and Department of Geoscience, University of Nevada, Las Vegas, Nevada 89154, USA

[c] Jet Propulsion Laboratory, California Institute of Technology, Pasadena, California 91109, USA

[d] GSECARS, University of Chicago, Argonne National Laboratory, Argonne, Illinois 60439, USA

[e] Hawai ῖ Institute of Geophysics and Planetology, School of Ocean and Earth Science and Technology, University of Hawai ῖ at Mānoa, Honolulu, Hawai ῖ 96822, USA

[f] Planetary Geosciences Institute, Department of Earth and Planetary Science, University of Tennessee, Knoxville, Tennessee 37996, USA

ABSTRACT

Tissintite (IMA 2013-027), $(Ca_{0.45}Na_{0.31}\square_{0.24})(Al_{0.97}Fe_{0.03}Mg_{0.01})(Si_{1.80}Al_{0.20})O_6$, is a new mineral that is a vacancy-rich, high-pressure clinopyroxene, with a composition equivalent to plagioclase. It occurs in maskelynite included within, or in contact with, shock melt pockets in the Tissint meteorite, a depleted olivine-phyric shergottite fall from Mars. Tissintite is a *C2/c* clinopyroxene, containing 42 – 60 mole % of the Ca-Eskola component, by far the highest known. The cell parameters are a = 9.21(17) Å, b = 9.09(4) Å, c = 5.20(2) Å, β = 109.6(9)°, V = 410 (8) $Å^3$, Z = 4. The density is 3.32 g/cm^3 and by combining cell parameters for tissintite with those from structure refinements of clinopyroxenes with lower vacancy concentrations, we estimate a cell volume for the Ca-Eskola end-member pyroxene

as 411±13 Å^3. At least in *C*2/*c* clinopyroxenes as sodic as tissintite, the a- and b- cell parameters as a function of vacancy concentration intersect at ~0.3 vacancies *pfu*, much lower than the Ca-Eskola end-member (0.5). Limiting concentrations of vacancies in the clinopyroxene structure as a function of Na/Ca and the stability field of tissintite are unknown but the inversion of anisotropy suggests an elastic instability that drives clinopyroxene toward a disordered trigonal structure closely related to that of wadeite; it may mark the boundary beyond which the breakdown of vacancy-rich clinopyroxene to a wadeite-structured phase + stishovite becomes stable.

Tissintite is a "goldilocks" phase, forming during a shock event severe enough to allow nucleation and growth of vacancy-rich clinopyroxene, probably from a melt of not too calcic and not too sodic plagioclase composition, but not so severe a shock that other high-pressure phases could grow and either destroy the clinopyroxene or buffer the vacancies to much lower values, thereby transforming high-vacancy tissintite into a low-vacancy clinopyroxene such as jadeite or kushiroite plus one or more additional phases. The kinetics for nucleation and growth of tissintite are probably slower for more-sodic plagioclase precursors, so tissintite is most likely to occur in depleted olivine phyric shergottites like Tissint and other highly shocked meteorites and lunar and terrestrial rocks that consistently contained calcic plagioclase precursors in the appropriate compositional range.

Keywords: Tissintite, (Ca,Na,□)$AlSi_2O_6$, new high-pressure pyroxene, clinopyroxene group, Ca-Eskola, Tissint meteorite, martian shergottite, synchrotron diffraction.
*E-mail: chi@gps.caltech.edu

1. Introduction

Because much of the Earth's interior lies hidden from view, we are left to infer its physical conditions, mineralogy, and bulk compositions through interpretation of seismic events, experiments on analog materials, theoretical modeling, examination of natural materials that sampled these regions, and by characterizing natural materials subjected to unusual processes. All of these venues can lead to a better understanding of the nature of planetary interiors (e.g.,

Akaogi, 2007; Ahrens et al., 2009; Stixrude and Lithgow-Bertelloni 2012; Hirose et al., 2014; Litvin et al., 2014). Minerals produced in shock events can be particularly useful, because of their potential for constraining the severity of the shock and, more generally, the properties of phases at high pressures and temperatures (e.g., Stöffler et al., 1991; Ohtani et al., 2004; Sharp and DeCarli, 2006, Walton et al., 2014). In this study, we describe a new mineral, "tissintite," with a shock-induced clinopyroxene structure which has a plagioclase equivalent composition, $(Ca,Na,\square)AlSi_2O_6$, requiring an extraordinarily large concentration of vacancies in roughly one quarter of the M2 sites. It is potentially an important indicator of the shock-metamorphic processes that generated martian meteorites and other highly shocked rocks.

Tissintite was discovered in and is named after the martian meteorite Tissint, which fell near Tissint, Morocco on 18 July 2011. Tissint is a fresh, olivine-phyric shergottite with strong-shock features and has been subjected to intense study since its fall (e.g., Aoudjehane et al., 2012; Baziotis et al., 2013; Herd et al., 2013; Udry et al., 2013; Walton et al., 2014). The mineral and its name (tissintite) were approved by the Commission on New Minerals, Nomenclature and Classification (CNMNC) of the International Mineralogical Association (IMA 2013-027) (Ma et al., 2013a). Ma et al. (2014) give a preliminary report of the results of this study.

2. Sample and analytical methods

2.1 Type material

Tissintite was identified in sections UT1, UT2 and UT3 (e.g., Figs. 1-2; formerly referred to as MT-1, 2, 3 by Baziotis et al., 2013) prepared at the University of Tennessee from a Tissint fragment with partial fusion crust. Type material in all three sections was deposited in the Meteorite Collection of the Frank H. McClung Museum at the University of Tennessee, Knoxville, Tennessee 37996, USA. Based on the common occurrence of tissintite in each of these sections, tissintite is likely to occur in most samples of the Tissint meteorite.

2.2 Analytical methods

Electron probe microanalysis (EPMA), high-resolution scanning electron microscopy (SEM), electron back scatter diffraction (EBSD), synchrotron X-ray diffraction, and microRaman analyses were used to determine the composition of tissintite, its physical

properties and structure, and to characterize associated phases. Back-scatter electron (BSE) imaging was performed using a ZEISS 1550VP field emission SEM. The EBSD analyses were performed using an HKL EBSD system on the ZEISS 1550VP SEM, operated at 20 kV and 6 nA in focused-beam mode with a 70 ºtilted stage and variable pressure mode (15 Pa). Chemical analyses of type tissintite and associated minerals were determined using a JEOL 8200 electron microprobe (WDS: 15 kV; 5 nA; beam in focused mode) interfaced with the Probe for EPMA program from Probe Software, Inc. Standards for the analysis were anorthite (Si*K*α, Al*K*α, Ca*K*α); albite (Na*K*α); fayalite (Fe*K*α); forsterite (Mg*K*α); Mn_2SiO_4 (Mn*K*α); TiO_2 (Ti*K*α); Cr_2O_3 (Cr*K*α); and microcline (K*K*α). Quantitative elemental microanalyses were processed with the CITZAF correction procedure (Armstrong, 1995), and analytical results are given in Table 1.

Diffraction data were collected at the undulator beamline 13-IDD (GSECARS, APS, Argonne National Laboratory) and at the superconducting bending-magnet beamline 12.2.2, (ALS, Lawrence Berkeley National Laboratory), using a primary beam energy of 37 keV (0.3344 Å) and 30 keV (0.4133 Å). The uncoated thin section UT2 was examined with no additional preparation. At the 13-IDD location, single crystal diffraction data of tissintite crystallites were collected with an X-ray beam focused to ~ 3×4 μm^2 by vertical and horizontal Kirkpatrick-Baez mirrors. A MAR165 CCD detector was used for collecting image frames in forward geometry, using 0.5 degree increments for the phi axis, while chi and theta angles of reflections were internal detector coordinates. The GSE_ADA software package (Dera et al., 2013) was used for data collection, peak-search, peak-fitting, correction of polarization, and for peak-integration. The RSV (Dera et al. 2013) was used for indexing and to export of hkl-files. A complementary set of diffraction data was collected at beamline ALS 12.2.2, with a beam of 15×20 μm^2 area, in order to acquire a powder-like diffraction pattern for tissintite.

Raman spectroscopic microanalysis was conducted using a 514.3 nm solid-state laser in a Renishaw M1000 micro-Raman spectrometer system on type tissintite in section UT2, using methods described in Ma and Rossman (2008, 2009). The spot size was ~2 μm.

3. Results

3.1 Occurrence, appearance, physical and optical properties

The Tissint "rock" contains mostly zoned olivine and pyroxene (mainly pigeonite), with minor chromite and ilmenite, plus shock-melt pockets. An assortment of shock-related phases

was reported. This includes ahrensite, akimotoite, diamond, jadeite, lingunite, majorite, maskelynite, stishovite, tuite, ringwoodite, and xieite (Baziotis et al., 2013; El Goresy et al., 2013a, 2013b; Kuchka et al., 2013; Ma et al., 2014; Walton et al., 2014). The new high-pressure mineral, ahrensite (Fe analog of ringwoodite, γ-$(Fe,Mg)_2SiO_4$, IMA 2013-028) (Ma et al., 2013b) occurs after olivine in ferroan rims on olivine phenocrysts, where the rim contacts a melt pocket.

Tissintite occurs in two basic textural forms, both consisting of fine-grained aggregates in maskelynite. The aggregates are composed of elongate to irregularly shaped single crystals, ranging from 100 nm in diameter up to $2 \times 2 \times 4$ μm^3 in size, with aspect ratios in the plane of the section of ~1 to ~10 and no coexisting crystalline phases. In the first textural style (Fig. 1), crystals form wormy intergrowths within a matrix of maskelynite and cellular tissintite. This tissintite - glass assemblage is completely enclosed by the host melt pocket. In a second textural type (Fig. 2), the precursor maskelynite is in contact with, but may not be completely enclosed by the melt pocket. Here, tissintite forms rims separating maskelynite from the contacting shock-melt pocket. There may be additional aggregates of tissintite forming inclusions within the glass (Fig. 2c). Note in Fig. 2c (also true of other occurrences), that maskelynite more than ~25 μm from the shock-melt pocket shows no tissintite; this is a conservative upper limit because shock-melt closest to a tissintite aggregate may well have been out of the plane of the thin section. For reasons of simplicity we use the term 'maskelynite' in this paper for any non-crystalline material with feldspar composition and indistinctive on whether the material is quenched melt or diaplectic glass.

3.2 Chemical composition and crystallography

The compositions of tissintite and associated maskelynite are given in Table 1. The type tissintite has an empirical formula [based on 6 oxygen atoms per formula unit (*pfu*)] of $(Ca_{0.45}Na_{0.31}\square_{0.24})(Al_{0.97}Fe_{0.03}Mg_{0.01})(Si_{1.80}Al_{0.20})O_6$, leading to a general formula of $(Ca,Na,\square)Al(Si,Al)_2O_6$. Compositions of tissintites observed in this study are fairly close to $(Ca_{1/2}Na_{1/4}\square_{1/4})(Al)(Al_{1/4}Si_{7/4})O_6$ with Ca#s, 100*Ca/(Ca + Na) on a molar basis, ranging from 58 to 69, and vacancy concentrations based on the stoichiometry, from 0.21 - 0.30 sites *pfu*. Compositions are consistent with vacancies being restricted to the M2 site with nearly full

occupancy of M1 by Al. Tissintite compositions are quite close to those of plagioclase. For the same composition, we can describe the connection between the two as

$$\frac{3}{4}(Ca_xNa_{1-x})(Al_{1+x}Si_{3-x})O_{8(plagioclase)} =$$
$$\left(Ca_{3x/4}Na_{(1-x)/4}\square_{1/4}\right)(Al)\left(Al_{(3x-1)/4}Si_{3(3-x)/4}\right)O_{6(clinopyroxene)}.$$

This relation holds for $1 \geq x \geq 1/3$ (i.e., for An33.3 – An100). If $x < 1/3$, negative amounts of tetrahedral Al are required. For tissintite restricted to the equivalent albite – anorthite join, a likely Na-free end-member is $(Ca_{3/4}\square_{1/4})Al(Si_{1.5}Al_{0.5})O_6$, where 1/4 of the M2 sites are vacant. The Ca-Eskola molecule, $(Ca_{1/2}\square_{1/2})AlSi_2O_6$, is a possible Ca-endmember for tissintite where half of the M1 sites are vacant.

Synchrotron diffraction was used to constrain the crystallographic properties of tissintite. The observed reflections arose from a mixture of phases, primarily fayalite and pigeonite from nearby quenched shock melt, and tissintite. We first indexed the reflections of coexisting fayalite crystals. Of the remaining reflections, 27 were found to belong to one crystallite of monoclinic symmetry with cell dimensions of a = 9.2 (2) Å; b = 9.09 (4) Å; c = 5.20 (2) Å; and β = 109.6 (9) Å, where one sigma errors are given inside parentheses. This unit cell in combination with the assignment of space group C2/c matches the EBSD pattern of tissintite with a mean angular deviation < 0.34 °. In contrast, the space groups $P2_1/c$ (pigeonite) or $P2/n$ (ordered omphacite) cannot fit the EBSD pattern.

The number of unique reflections belonging to this and other individual crystallites of tissintite was too small for structure analysis. Moreover, some of the observed intensities appear to be affected by extinction from major reflections of coexisting phases in the examined sample (i.e., fayalite and pigeonite). We can nevertheless compute the density of tissintite as 3.32 g/cm^3 from these cell parameters and the composition given in Table 1.

Micro-synchrotron X-ray diffraction patterns of multicrystal-multiphase aggregates frequently suffer from extinction by coexisting phases; this effect can be compensated for by large statistics of reflections but these are not available for tissintite. We therefore collected a complementary set of synchrotron diffraction data at beamline ALS 12.2.2, with a beam of 15×20 μm^2 area, and the intent of acquiring a powder-like diffraction pattern for tissintite.

However, this dataset also evades a fully quantitative interpretation because of the prominent texture of the tissintite aggregates (e.g., Figs. 1-2) and the superimposition of reflections from an array of adjacent pigeonite crystallites, which cannot be well accounted for by Rietveld refinement or masking (Hammersley et al. 1996). Although the different weight of overlapping reflections in textures of polycrystals can be assessed, the overlap of the pattern of tissintite with sporadic single crystal reflections of adjacent pigeonite limited the possibility of fitting the aggregate texture.

Absent a more comprehensive dataset for tissintite, the internal structural parameters, such as the vacancy distribution between M1 and M2, cannot be fully assessed because they correlate to a large extent with crystallite orientations. We optimized for this textural effect by fitting using spherical harmonics (Von Dreele, 1997) for the two extreme cases of all vacancies on M2 (Ca-Eskola molecule) and all vacancies on M1. The Rietveld refinements slightly favor the Ca-Eskola molecule, with an Rwp (Rietveld weighted profile factor) of 9.0% over a model with vacancies relegated to the M1 site, which yields an Rwp of 10.5%. We note that a structure model with ~50 – 60% Ca-Eskola molecule in tissintite is clearly supported by the cell parameters and volume as shown in the Supplement. Reflections attributable to stishovite were not observed.

The Raman spectrum of type tissintite, shown in Fig. 4, is similar to that of jadeite with major features at 203; 377; 415; 523; 572; 693; and 1000 cm^{-1}. These features are consistent with both experimental and theoretical expectations for a *C2/c* clinopyroxene (e.g., Yang et al., 2009; Prencipe, 2012), but noticeably broader than is typical of clinopyroxene reference phases. For example, the full-width at half-height of the 693 cm^{-1} tissintite band is about 25 cm^{-1} compared to the corresponding jadeite band at 700 cm^{-1} that is 9 cm^{-1} wide. In the jadeite spectrum, there is a pair of sharply defined bands near 1000 cm^{-1}. In tissinitite, there is a single broad band of about 83 cm^{-1} width. These anomalous widths are indicative of cation disorder in the tissintite structure (e.g., Ca-Na on the M2 site). As Fig. 3 indicates, the Raman spectrum of tissintite is inconsistent with either maskelynite or plagioclase.

4. Discussion

Tissintite is a clinopyroxene, $(Ca,Na,\square)AlSi_2O_6$, in which the M1 site is completely (or almost so) occupied by Al. It can be thought of as the Ca-analog of jadeite with ~¼ of the M2

sites being vacant, with a likely Ca-end member of $(Ca_{3/4}\square_{1/4})Al(Si_{3/2}Al_{1/2})O_6$ for an anorthite-equivalent composition, or with greater vacancy concentrations, a Ca-Eskola component (CaEs: $(Ca_{1/2}\square_{1/2})AlSi_2O_6$). The connection between tissintite with a Ca# of 2/3 and other pyroxene components can be considered as:

$$(Ca_{1/2}Na_{1/4}\square_{1/4})Al_{5/4}Si_{7/4}O_6 = \tfrac{1}{2}\,(Ca_{1/2}\square_{1/2})AlSi_2O_6 + \tfrac{1}{4}\,NaAlSi_2O_6 + \tfrac{1}{4}\,CaAl_2SiO_6$$

or

tissintite = ½ Ca-Eskola + ¼ jadeite + ¼ kushiroite.

Tissintite is quite aluminous (~30 wt% Al_2O_3), but kushiroites are more so (up to 46 wt%; Ma et al., 2009), and it is the extraordinarily high vacancy concentration on the M2 site that is the salient structural characteristic. In the sections we studied, 21 to 30 % of the M2 sites are vacant, making tissintite the most highly defective natural clinopyroxene reported to date. By comparison, less than 10 % of the M2 sites are vacant in clinopyroxenes from mantle xenoliths (e.g., Oberti and Caporuscio, 1991; Smyth, 1980). It has been argued that substantially higher vacancy concentrations were achieved in symplectites from ultra-high-pressure metamorphic rocks, but if so, they shed vacancies during decompression, perhaps through the commonly observed exsolution of silica (e.g., Katayama et al., 2000). Tissintite also exhibits more vacancies than any synthetic clinopyroxene, of which we are aware. Zhao et al. (2011) reported synthesizing aluminous clinopyroxenes with up to ~20 % vacancies on M2, but <10 % is more typical of clinopyroxenes in experimental run products with mantle phase assemblages (e.g., Irifune et al., 1986; Konzett et al., 2008; Pertermann and Hirschmann, 2002). If vacancies on M2 are accounted for through the Ca-Eskola component, as is typical for work on ultra-high pressure metamorphism and the petrology of the upper mantle, then tissintites have 42 – 60 % Ca-Eskola component. This is up to 50 % more than concentrations observed in the most vacancy-rich synthetic clinopyroxene and several times the values in other natural clinopyroxenes. Although inaccuracies of the measured cell parameters are large, the values are consistent with expectations for a vacancy-rich *C2/c* clinopyroxene, as shown in Fig. 4. Cell parameters and volumes of *C2/c* clinopyroxenes are a strong function of Ca# (e.g., Wood et al., 1980) and, since Ca# = 59 for the type tissintite, we show cell parameters and volumes for tissintite in Fig. 4 along with those of natural *C2/c* clinopyroxenes with 54 < Ca# < 64 from

McCormick (1986), Oberti and Caporuscio (1991), and Nestola et al. (2007) as a function of vacancy concentration on the M2 site. We used data from these sources rather than computing deviations of cation sums from 4 *pfu* because the structure analyses provide a more direct measurement of vacancy concentrations. Fig. 4a shows linear correlations between vacancy concentrations and axis lengths, although there is a hint of nonlinearity for b. The correlation between volume and vacancy concentration (Fig. 4c) is also linear within the scatter of data. The data for β at very low vacancy concentrations (Figs. 4b) indicate that β decreases with increasing concentration of vacancies but this negative slope must reverse at higher concentrations to be consistent with β in tissintite. In the Supplement, we estimate the cell volume of the Ca-Eskola molecule as 411 ± 13 $Å^3$ for the Ca-Eskola end-member using these data, which is potentially larger but, within error, consistent with McCormick's (1986) assessment of 402 ± 5 $Å^3$.

An important feature of the trends shown in Figs. 4a-c is that the a- and b-axes intersect at a vacancy concentration of ~ 0.3 *pfu* and an axis length of ~9.15 Å, keeping in mind that the large error in the a-axis length of tissintite makes the precise location of the intersection rather uncertain. This 'inversion' of unit cell anisotropy does not require but is often associated with a structural instability, so we examine whether or not a convergence of the a- and b-axis lengths can induce a instability in vacancy-rich clinopyroxenes. A first observation is that equality of the a- and b-axes in tissintite makes the unit cell equivalent to a *C*-centered orthorhombic cell, which in turn can be interpreted as a subgroup of a trigonal cell. An equivalent structure is obtained by a direct group-subgroup relationship between $C2/c$ and $P\bar{3}1c$ with transformation matrix (0 0 1| -½ ½ 0| 0 0 1), which maintains the axis lengths of the monoclinic cell but increases the angle from ~ 110 to 120°. The trigonal structure has higher multiplicities for all atoms and, therefore, the atoms are disordered on these high symmetry sites with partial occupancies. This is a purely geometric mapping, but two points are noteworthy:

1) The trigonal structure is related to the clinopyroxene structure through condensation *only* of zone center modes (Table 3). This means the transition can occur spontaneously without diffusion and it can be of second order if the monoclinic angle approaches 120° at elevated temperature.
2) The trigonal structure has a marked resemblance to the structure of the wadeite-benitoite group and, in particular to the known high pressure decomposition product of feldspars $(K,Na)_2AlSi_2O_9$ (e.g., Kinomura et al. 1975; Yagi et al. 1994) It is plausible that a

disordered trigonal structure is transient to decomposition of the vacancy-rich pyroxene to a wadeite-type silicate plus a high pressure silica polymorph. Unlike the monoclinic - trigonal transition described above, however, this process involves the diffusion of atoms. These two points taken together suggest that there is an upper limit to the Ca-Eskola component in clinopyroxenes. For a Ca# ~60, this limit is ~0.3 M2 vacancies *pfu*. The most vacancy-rich of the tissintites in Tissint, which are the most vacancy-rich clinopyroxenes currently known, are close to this limiting concentration but experimentation on bulk compositions off the albite-anorthite join would probably be required to test the proposed limit. The corresponding vacancy limit for Ca# = 100 (i.e. for the Ca-Eskola end member) is unknown but it is possible that the Ca-Eskola molecule is not a physically attainable phase.

In addition to structural constraints limiting concentrations of vacancies on the M2 site in clinopyroxene, there are charge balance restrictions. In Fig. 5, we show Ca# [molar Ca/(Ca+Na)] as a function of vacancy concentration on the M2 site. In this plot, we assign monovalent cations to M2 and assume that all vacancies are also on this site, with all other defects being present in negligible amounts. If the M1 site is then occupied only by trivalent and divalent cations (i.e., ignoring Ti), the maximum concentration of vacancies at any given Ca# is defined by an M1 site fully occupied by trivalent cations and tetrahedral sites fully occupied by Si. This leads to a curve defining a charge balance limit for M2 vacancies that extends from the origin (end-member jadeite) to the Ca-Eskola component for a Ca# of 100. Clinopyroxenes have compositions plotting on or above this curve. A survey of experimental data from the literature encompassing simple to complex natural systems (references given in the caption to Fig. 5) yields a broad range of vacancy concentrations, depending on bulk composition, temperature, and pressure, but nearly all lie above the limiting vacancy curve. We interpret values beyond the hypothetical limit (two analyses from Massone and Fockenberg, 2012) to be analytical artifacts and probably within analytical error of being consistent with the vacancy limit. Note also that the limiting curve shown in Fig. 5 refers to full occupancy of M1 by trivalent cations; if the M1 site contains divalent cations, as it frequently does in high-pressure pyroxenes, then additional monovalent cations on M2 are required for charge balance, which further reduces the number of potentially available vacancies on the M2 site.

In Fig. 5, tissintite compositions plot close to the plagioclase join, well above the vacancy limit curve but with higher vacancy concentrations than observed in phase-equilibria studies

(gray region in Fig. 5). Compositions of tissintites (Fig. 5) showing wormy intergrowths (e.g., Fig. 1) overlap those of rimming textural types (e.g., Fig. 2), suggesting that differences in composition are not at the root of the different textures. It seems likely that the basic formation mechanism for the two textural types is the same and we, therefore, discuss their origin together.

We take three fundamental observations from the above descriptions. Tissintite forms from a plagioclase composition material (i.e., bulk compositions in the system of greatest interest lie along the anorthite-albite join); it has a near-feldspar equivalent composition; there are no additional crystalline phases. In particular, no silica polymorph, garnet, corundum, aluminosilicate (e.g., kyanite), CAS phase, or hollandite-structured phase like lingunite is observed coexisting with tissintite. Phase equilibria for plagioclases of intermediate composition have not been studied in detail at high pressures and temperatures, so we first consider expectations based on the end-members albite and anorthite and then experiments conducted on bulk compositions off the plagioclase join. Finally, we evaluate the data of Kubo et al. (2010) on labradorite (An 58).

Above ~3 GPa, albite breaks down to form jadeite (i.e., a low-vacancy clinopyroxene) plus quartz or a silica-rich liquid, and the jadeite is unstable relative to wadeite-structured $Na_2AlSi_2O_9$ plus stishovite or a $CaFe_2SiO_4$-structured $NaAlSiO_4$ plus stishovite lingunite, the hollandite-structured form of $NaAlSi_3O_8$ above ~17 GPa (e.g., Liu, 1978; Presnall, 1995; Tutti et al., 2000; Tutti, 2007). Thus, based solely on the phase diagram for albite, a plausible origin for tissintite would be as a stable liquidus phase crystallizing from a plagioclase composition liquid at shock pressures within the liquidus phase field of clinopyroxene (<~17 GPa for an albite bulk composition) with rapid quenching to prevent nucleation and growth of other phases. In this scenario, plagioclase enclaves within shock melt pockets and those portions of large maskelynites closest to shock melt pockets melted, as proposed by El Goresy and coworkers (Chen and El Goresy, 2000; El Goresy, 2013a), and the tissintite crystallized as the liquidus phase from these melts. Portions of maskelynites further than ~25 μm from a melt pocket either didn't melt or were not heated sufficiently to allow for crystallization of tissintite. This mode of origin is attractive in its simplicity but caution must be exercised in extrapolating expectations based on albite all the way to the ~An65 relevant to tissintite and, even if one were to do so, it provides no basis for asserting that tissintite, rather than a low-vacancy clinopyroxene is the stable liquidus phase. Clinopyroxene is not stable at all for an anorthite bulk composition;

instead anorthite at low pressures and temperatures yields to a melt of anorthite composition, and various phase assemblages involving two or more phases, including corundum; grossular; kyanite; stishovite; $CaSiO_3$ perovskite; and the CAS phase, $CaAl_4Si_2O_{11}$ (Presnall, 1995; Liu et al. 2012). Based solely on data for the anorthite bulk composition, tissintite is not a stable phase, so there must be an upper limit to the Ca# of tissintite on the plagioclase join. Moreover, based on a fairly large collection of experiments described in the literature (sources given in the caption to Fig. 5), clinopyroxene coexisting with another crystalline phase will have a much lower vacancy concentration than tissintite. If this holds generally, then tissintite is always metastable, outside a primary phase field for clinopyroxene, relative to a phase assemblage that either contains no clinopyroxene or one that contains a low-vacancy clinopyroxene (i.e., not tissintite). Thus, one key to the presence of tissintite appears to be the absence of any other crystalline phases.

Kubo et al. (2010) investigated the amorphization of and crystallization in a natural labradorite (An58) through *in situ* multi-anvil experiments at 8 – 26 GPa and relatively low temperatures (<~1000 ℃). The starting material was somewhat more sodic than our tissintite (Ca#~65), although quite close to that of the type material (Ca# = 59). In one set of experiments, Kubo et al. (2010) cold-pressurized the plagioclase and then heated it (see solid lines in Fig. 6). The rate was not specified, but this is unimportant for the purposes of illustration. As the temperature increased from low levels, plagioclase became x-ray amorphous and, as heating continued, clinopyroxene of unknown composition nucleated and grew, and, finally, garnet and/or stishovite crystallized. A key result of Kubo et al. (2010) is that the clinopyroxene (tissintite?) was the first crystalline phase to nucleate in their experiments but that other phases have faster growth rates. The experiments refer to subsolidus conditions but the same nucleation advantages likely hold for crystallization from a melt and, indeed, may be even greater than implied by the experiments if their clinopyroxenes were vacancy-poor. The work of Kubo et al. suggests an alternative to liquidus phase crystallization as a mechanism for the formation for tissintite through nucleation and growth in the solid-state, or from a melt if tissintite is not on the liquidus, under conditions that prevented nucleation and growth of any other crystalline phases. If plagioclase melted, as championed by Chen and El Goresy (2000) and El Goresy et al. (2013a) for shergottites in general and El Goresy et al. (2013b) for Tissint, in particular, and tissintite crystallized from the melt, then quenching must have been sufficiently fast that no other phase

could crystallize during cooling. Any interaction of such phases with tissintite would have destroyed the vacancies and, thereby, destroyed the tissintite in favor of a low-vacancy clinopyroxene or some other phase(s). In this scenario, tissintite either crystallized during heating of maskelynite and the plagioclase did not melt, or, more likely, tissintite crystallized during cooling of a liquid as other phases failed to nucleate. We note in the latter context that tissintite is only present in maskelynite enclosed by or within ~25 μm of a melt pocket, either indicating that only those portions of the maskelynite melted or, if all were melted as claimed by El Goresy et al. (2013a), only these regions were heated sufficiently to support the growth of tissintite. Otherwise, tissintite would be ubiquitous in Tissint maskelynites, independent of distance from melt pockets, instead of being so spatially restricted. Although growth of tissintite is probably diffusion limited (maskeleynite is invariably slightly more sodic than coexisting tissintite), the required changes in composition are very small compared to those required for low vacancy clinopyroxenes or other phases and dominated by Na, a fast diffusing cation.

Another important point to be gleaned from the experimental study of Kubo et al. (2010) is that clinopyroxene and subsequent phases crystallize much faster in amorphous labradorite than in amorphous albite, at the same pressures and temperatures. If this holds generally, then more-sodic plagioclase requires greater shock intensities to produce tissintite, and should it do so, there is more time at elevated pressures and temperature for additional phases to appear that would destroy the tissintite. Once formed, a calcic tissintite is more likely to survive. Finally, we note that our framing of Kubo et al. (2010) in this discussion is qualitative, but tissintite is a phase of immense potential for constraining shock conditions. Tissintite of a given composition can only form over a small range of P-T-t. With experimental calibration, tissintite may provide explicit statements of conditions during the shock event.

Tissintite has, to our knowledge, never been synthesized, although it is possible that some experiments of Kubo et al. (2010) produced this phase. Thus, the conditions under which tissintite formed cannot be guided by currently available experiments on this phase. Nevertheless, tissintite in the Tissint meteorite is most readily explained as a shock-induced phase that crystallized from plagioclase composition melts, either as the stable liquidus phase or as a metastable but rapidly nucleating phase that survived because more stable phases were unable to nucleate and grow during the shock event. Tissintite only occurs in maskelynite enclaves within shock-induced melt-pockets or in portions of maskelynite at or very close to

contacts with melt pockets. Thus, the high P-T associated with melt pockets is a requirement for the formation of tissintite. The composition of tissintite is essentially equivalent to that of plagioclase, but it is slightly more sodic than coexisting plagioclase glass, implying fractionation during growth, which is more readily accomplished in a shock event through crystallization from a melt than a glass.

As noted above in discussing Fig. 5, tissintite cannot form in sodic plagioclase precursors (<An33), so based on observed plagioclase compositions (Brearley and Jones, 1998; Mittlefeldt et al., 1998), tissintite is unlikely to be found in highly equilibrated ordinary chondrites, enstatite achondrites, lodranites, or acapulcoites, although it is certainly possible, for example, for low-vacancy jadeites to form where these types of meteorites are highly shocked, as is observed in ordinary chondrites (Miyahara et al., 2013 and references therein). Similarly, plagioclase in many terrestrial impact sites is too sodic to produce tissintite [e.g., the clinopyroxenes in ~An20 maskelynites from the Ries crater (James, 1967) are jadeites and not tissintites]. The maximum Ca# for a plagioclase that can potentially yield tissintite is unknown beyond being <An100 but feldspars in Ca-, Al-rich inclusions from carbonaceous chondrites are probably too calcic [typically, An99-100; Brearley and Jones (1998)]. There are, however, many potential target rocks with plagioclase compositions more appropriate for the formation of tissintite. Plagioclase is ~An55 at the terrestrial Manicouagan impact site in Quebec (White, 1993). Calcic igneous plagioclase with An60-An85 is observed in ferromagnesian and Al-rich chondrules from carbonaceous, enstatite, R, and unequilibrated and moderately equilibrated ordinary chondrites (Brearley and Jones, 1998). Most of these meteorites are only lightly shocked (or annealed after heavy shocks) but, where heavily shocked, tissintite is a possibility. Plagioclase in lunar rocks is generally quite calcic and some lunar meteorites are heavily shocked (Papike et al., 1998; Lin et al., 2012), so tissintite may well occur in them.

In martian meteorites, the Ca# in maskelynite ranges from ~20 to ~70 (e.g., Fritz et al., 2005; Papike et al., 2009). There is no prohibition based on the M2 vacancy-limit shown in Fig. 5 to prevent substantially more sodic tissintites than observed. We postulate that one limitation on the occurrence of tissintite is that the vacancy concentration at which axis length inversion occurs in clinopyroxene (e.g., Fig. 4a) decreases with decreasing Ca#. If so, observed tissintites in Tissint may be close to the sodic limit. The apparent absence of tissintite in most martian meteorites may also reflect differences in formation conditions but the most important factor is

likely to be the composition of maskelynite adjacent to shock melt pockets and veins. We note that the most calcic maskelynite in a given shergottite generally occurs in the core region of the precursor crystals and these may not have been heated sufficiently to form tissintite (of course, tissintite may exist in some of these meteorites but has been overlooked). Thus, the most promising candidates for tissintite in martian meteorites are the depleted olivine-phyric shergottites (NWA 4925, NWA 5789, NWA 5990, and Tissint of which we have only investigated Tissint), where most of the maskelynite is more calcic than An60, and shock intensities may have been similar.

Conclusions

Tissintite, $(Ca,Na,\square)AlSi_2O_6$, is an extraordinarily vacancy-rich, dense clinopyroxene with a plagioclase equivalent composition that formed in the Tissint martian meteorite during a shock event. The a- and c-axes of vacancy-bearing clinopyroxenes contract with increasing vacancy concentration and the overall effect of the vacancies is contractive (i.e., cell volumes decrease with increasing vacancy concentration). At vacancy concentrations of ~0.3 *pfu* for clinopyroxene with Ca# ~60, the a- and b- axes lengths intersect and a spontaneous elastic instability with transition to a disordered trigonal structure is possible. This trigonal structure has a strong structural similarity to the wadeite-structure and it is conceivable that it represents a transient to decomposition of vacancy-rich clinopyroxenes to (Ca,Na)Al-wadeite plus stishovite. If this effect is also true of clinopyroxenes more calcic than tissintite, then the Ca-Eskola end-member may not be physically realizable or is, at the least, energetically highly unfavorable. Tissintite crystallized during a shock event that was severe enough to allow its nucleation and growth after plagioclase precursors in or near shock melt pockets, but not so severe that other phases, which would have destroyed the tissintite, could nucleate and grow.

Acknowledgements

SEM, EBSD and EPMA analyses were carried out at the Caltech GPS Division Analytical Facility, which is supported, in part, by NSF Grants EAR-0318518 and DMR-0080065. Synchrotron diffraction was carried out at the 13-IDD beamline of the Advanced Photon Source and the 12.2.2 beamline of the Advanced Light Source. Use of the Advanced Photon Source, an Office of Science User Facility operated for the U.S. Department of Energy

(DOE) Office of Science by Argonne National Laboratory, was supported by the U.S. DOE under Contract No. DE-AC02-06CH11357**.** The Advanced Light Source is supported by the Director, Office of Science, Office of Basic Energy Sciences, of the U.S. Department of Energy under Contract No. DE-AC02-05CH11231. OT acknowledges the support from DOE Cooperative Agreement #DE-NA0001982. PD and GRR acknowledge NSF EAR grants 1344942 and 322082 respectively. LAT and JRB acknowledge NASA Cosmochemistry grants NNX11AG58G and NNX12AH63G, respectively. Formal reviews by A. El Goresy and an anonymous reviewer and additional comments by T. Kubo all led to significant improvements.

References

Ahrens, T.J., Asimow, P.D., Mosenfelder, J.L., 2009. Advances in shock compression of mantle minerals and implications. AIP Conf. Proc. 1195, 859 (2009); doi: 10.1063/1.3295278.

Akaogi, M., 2007. Phase transitions of minerals in the transition zone and upper part of the lower mantle. In: Ohtani, E. (Ed.), Advances in High-Pressure Mineralogy: Geol. Soc. Amer. Spec. Paper 421, 1-13.

Akaogi, M., Haraguchi, M., Nakanishi, K., Ajiro, H., Kojitani, H., 2010. High-pressure phase relations in the system $CaAl_4Si_2O_{11}$ - $NaAl_3Si_3O_{11}$ with implication for Na-rich CAS phase in shocked Martian meteorites. Earth Planet. Sci. Lett. 289, 503–508.

Aoudjehane, H.C., Avice, G., Barrat, J.-A., Boudouma, O., Chen, G., Duke, M.J.M., Franchi, I.A., Gattacceca, J., Grady, M.M., Greenwood, R.C., Herd, C.D.K., Hewins, R., Jambon, A., Marty, B., Rochette, P., Smith, C.L., Sautter, V., Verchovsky, A., Weber, P., Zanda, B., 2012. Tissint Martian meteorite: A fresh look at the interior, surface, and atmosphere of Mars. Science 338, 785–788.

Armstrong, J.T., 1995. CITZAF: a package of correction programs for the quantitative electron microbeam X-ray analysis of thick polished materials, thin films, and particles. Microbeam Anal. 4, 177–200.

Baziotis, I.P., Liu, Y., DeCarli, P.S., Melosh, H.J., McSween, H.Y., Bodnar, R.J., Taylor, L.A., 2013. The Tissint Martian meteorite as evidence for the largest impact excavation. Nature Comm. 4:1404; DOI:10.1038/ncomms2414.

Brearley, A.J., Jones, R.H., 1998. Chondritic meteorites. Rev. Mineral. 36, 3-1 – 3-398.

Chen, M., El Goresy, A., 2000. The nature of maskelynite in shocked meteorites: not diaplectic glass but a glass quenched from shock-induced dense melt at high pressures. Earth Planet. Sci. Lett. 179, 489–502.

Dera, P., Zhuravlev, K., Prakapenka, V., Rivers, M.L., Finkelstein, G.J., Grubor-Urosevic, O., Tschauner, O., Clark, S.M., Downs, R.T., 2013. High pressure single-crystal micro X-ray diffraction analysis with GSE_ADA/RSV software. High Pressure Res. 33, 466–484.

El Goresy, A.,Gillet, Ph., Miyahara, M., Ohtani, E., Ozawa, S., Beck, P., Montagnac, G., 2013a. Shock-induced deformation of shergottites: shock-pressures and perturbations of magmatic ages on Mars. Geochim. Cosmochim. Acta 101, 233-262.

El Goresy, A., Gillet, Ph., Miyahara, M., Ohtani, E., Ozawa, S., Lin, Y., Feng, L., Escerig. S., 2013b. Multiple shock events and diamond formation on Mars. Lunar Planet. Sci. Conf. 44. 1037. pdf

Fritz, J., Greshake, A., Stöffler, D., 2005. Micro-Raman spectroscopy of plagioclase and maskelynite in Martian meteorites: Evidence of progressive shock metamorphism. Antarc. Meteorit. Res. 18, 96–116.

Gasparik, T., 1984. Experimentally determined stability of clinopyroxene + garnet + corundum in the system CaO-MgO-Al_2O_3-SiO_2. Am. Mineral. 69, 1025–1035.

Gasparik, T., 1985. Experimental study of subsolidus phase relations and mixing properties of pyroxene and plagioclase in the system Na_2O-CaO-Al_2O_3-SiO_2. Contrib. Mineral. Petrol. 89, 346–357.

Gasparik, T., 1986. Experimental study of subsolidus phase relations and mixing properties of clinopyroxene in the silica-saturated system CaO-MgO-Al_2O_3-SiO_2. Am. Mineral. 71, 686–693.

Hammersley, A.P., Svensson, S.O., Hanfland, M., Fitch, A.N., Hausermann, D., 1996. Two-dimensional detector software: From real detector to idealised image or two-theta scan. High Press. Res. 14, 235–248.

Herd, C.D.K., Duke, M.J.M., Bryden, C.D., Pearson, D.G., 2013. Tissint among the shergottites: Parental melt composition, redox state, La/Yb and V/Sc. Lunar Planet. Sci. Conf. 44. 2683. pdf

Hirose, K., Labrosse, S., Hernlund, J. 2014. Composition and state of the Earth's core. Ann. Rev. Earth Planet. Sci.41, 657-691.

Irifune, T., Sekine, T., Ringwood, A.E., Hibberson, W.O., 1986. The eclogite-garnetite transformation at high pressure and some geophysical implications. Earth Planet. Sys. 77, 245–256.

Ishii, T., Kojitani, H., Akaogi, M., 2012. High-pressure phase transitions and subduction behavior of continental crust at pressure-temperature conditions up to the upper part of the lower mantle. Earth Planet. Sci. Lett. 357–358, 31–41.

James, O.B., 1969. Jadeite: shock-induced formation from oligoclase, Ries crater, Germany. Science 165, 1005-1008.

Johnston, C.L., Gunter, M.E., Knowles, C.R., 1991. Sunstone labradorite from the Ponderosa Mine, Oregon. Gems & Gemology 27, 220–233.

Katayama, I., Parkinson, C.D., Okamoto, K., Nakajima, Y., Maruyama, S., 2000. Supersilicic clinopyroxene and silica exsolution in UHPM eclogite and pelitic gneiss from the Kokchetav massif, Kazakhstan. Am. Mineral. 85, 1368–1374.

Kimura, M., Mikouchi, T., Suzuki, A., Miyahara, M., Ohtani, E., El Goresy, A., 2009. Kushiroite, $CaAlAlSiO_6$: A new mineral of the pyroxene group from the ALH 85085 CH chondrite, and its genetic significance in refractory inclusions. Am. Mineral. 94, 1479–1482.

Kinomura, N., Kume, S., Koizumi, M., 1975. Stability of $K_2Si_4O_9$ with wadeite type structure. Proc. 4th Int. Conf. High Pressure Sci. Tech. 211–214.

Knapp, N., Woodland, A.B., Klimm, K., 2013. Experimental constraints in the CMAS system on the Ca-Eskola content of eclogitic clinopyroxene. Eur. J. Mineral. 25, 579–596.

Konzett, J., Frost, D.J., Proyer, A., Ulmer, P., 2008. The Ca-Eskola component in eclogitic clinopyroxene as a function of pressure, temperature and bulk composition: an experimental study to 15 GPa with possible implications for the formation of oriented SiO_2-inclusions in omphacite. Contrib. Mineral. Petrol. 155, 215–228.

Kubo, T., Kimura, M., Kato, T., Nishi, M., Tominaga, A., Kikegawa, T., Funakoshi, K., 2010. Plagioclase breakdown as an indicator for shock conditions of meteorites. Nature Geosci. 3, 41–45.

Kuchka, C.R., Walton, E.L., Herd, C.D.K., 2013. Shock melt features in Los Angeles and Tissint: A comparison. Lunar Planet. Sci. Conf. 44. 3043. pdf

Litvin, Y., Spivak, A., Solopova, N., and Dubrovinsky, L. (2014) On origin of lower-mantle diamonds and their primary inclusions. Phys. Earth Planet. Int. 228, 176-185.

Lin, Y., Shen, W., Liu, Y., Xu, L., Hofmann, B.A., Mao, Q., Tang, G.Q., Wu, F., Li, X.H., 2012. Very high-K KREEP-rich clasts in the impact melt breccia of the lunar meteorite SaU 169: New constraints on the last residue of the Lunar Magma Ocean. Geochim. Cosmochim. Acta 85, 19-40.

Liu, L.-G., 1978. High-pressure phase transformations of albite, jadeite and nepheline. Earth Planet. Sci. Lett. 37, 438–444.

Liu, X., Ohfuji, H., Nishiyama, N., He, Q., Sanehira, T., Irifune, T., 2012. High-*P* behavior of anorthite composition and some phase relations of the CaO-Al_2O_3-SiO_2 system to the lower mantle of the Earth and their geophysical implications. J. Geophys. Res. 117, B09205, doi:10.1029/2012JB009290.

Ma, C., Rossman, G.R., 2008. Barioperovskite, $BaTiO_3$, a new mineral from the Benitoite Mine, California. Am. Mineral. 93, 154–157.

Ma, C., Rossman, G.R., 2009. Tistarite, Ti_2O_3, a new refractory mineral from the Allende meteorite. Am. Mineral. 94, 841–844.

Ma, C., Simon, S.B., Rossman, G.R., Grossman, L., 2009. Calcium Tschermak's pryoxene, $CaAlAlSiO_6$ from the Allende and Murray meteorites: EBSD and micro-Raman characterizations. Am. Mineral. 94, 1483–1486.

Ma, C., Liu, Y., Tschauner, O., 2013a. Tissintite, IMA 2013-027. CNMNC Newsletter No. 16, August 2013, page 2707. Mineral. Mag. 77, 2695–2709.

Ma, C., Tschauner, O., Liu, Y., Sinogeikin, S., 2013b. Ahrensite, IMA 2013-028. CNMNC Newsletter No. 16, August 2013, page 2707. Mineral. Mag. 77, 2695–2709.

Ma, C., Tschauner, O., Liu, Y., Beckett, J.R., Rossman, G.R., Zuravlev, K., Prakapenka, V., Dera, P., Sinogeikin, S., Smith, J., Taylor, L.A., 2014. Discovery of ahrensite γ-Fe_2SiO_4 and tissintite $(Ca,Na,\square)AlSi_2O_6$: two new high pressure minerals from the Tissint Martian meteorite. Lunar Planet. Sci. Conf. 45. 1222. pdf

Massone, H.-J., Fockenberg, T., 2012. Melting of metasedimentary rocks at ultrahigh pressure—Insights from experiments and thermodynamic calculations. Lithosphere 4, 269–285.

McCormick T.C., 1986. Crystal-chemical aspects of nonstoichiometric pyroxenes. Am. Mineral. 71, 1434–1440.

Mittlefeldt, D.W., McCoy, T.J., Goodrich, C.A., Kracher, A., 1998.Non-chondritic meteorites from asteroidal bodies. Rev. Mineral. 36, 4-1 – 4-195.

Miyahara, M., Ozawa, S., Ohtani, E., Kimura, M., Kubo, T., Sakai, T., Nagase, T., Nishijima, M., Hirao, N., 2013. Jadeite formation in shocked ordinary chondrites. Earth Planet. Sci. Lett. 373, 102−108.

Nestola, F., Longo, M., McCammon, C., and Boffa Ballaran, T., 2007. Crystal-structure refinement of Na-bearing clinopyroxenes from mantle-derived eclogite xenoliths. Am. Mineral. 92, 1242−1245.

Oberti, R., Caporuscio, F.A., 1991. Crystal chemistry of clinopyroxenes from mantle eclogites: A study of the key role of the M2 site population by means of crystal-structure refinement. Am. Mineral. 76, 1141−1152.

Ohtani E., Kimura Y., Kimura M., Takata T., Kondo T., Kubo T., 2004. Formation of high-pressure minerals in shocked L6 chondrite Yamato 791384: constraints on shock conditions and parent body size. *Earth Planet. Sci. Lett*. 227, 505−515.

Okamoto, K., Maruyama, S., 2004. The eclogite-garnetite transformation in the MORB + H_2O system. Phys. Earth Planet. Int. 146, 283−296.

Ono, S., Yasuda, A., 1996. Compositional change of majoritic garnet in a MORB composition from 7 to 17 GPa and 1400 to 1600 ℃. Phys. Earth Planet. Int. 96, 171−179.

Papike, J.J., Ryder, G., Shearer, C. , 1998. Lunar samples. Rev. Mineral. 36, 5-1 – 5-234.

Papike, J.J., Karner, J.M., Shearer, C.K., Burger, P.V., 2009. Silicate mineralogy of martian meteorites. Geochim. Cosmochim. Acta 73, 7443−7485.

Pertermann, M., Hirschmann, M.M., 2002. Trace-element partitioning between vacancy-rich eclogitic clinopyroxene and silicate melt. Am. Mineral. 87, 1365−1376.

Prencipe, M. (2012) Simulation of vibrational spectra of crystals by ab initio calculations: an invaluable aid in the assignment and interpretation of the Raman signals. The case of jadeite ($NaAlSi_2O_6$). J. Raman Spectro. 43, 1567−1569.

Presnall, D.C., 1995. Phase diagrams of Earth-forming minerals. p. 248-268 in Ahrens, T. J. (ed.) Handbook of Physical Constants, Mineral Physics and Crystallography, Am. Geophys. Union, Washington, D.C.

Sharp T.G., DeCarli P.S., 2006. Shock effects in meteorites. In: Lauretta, D.S., McSween, H.Y. (Eds.), Meteorites and the Early Solar System II. University of Arizona Press, Tucson, pp. 653−677.

Smyth, J.R., 1980. Cation vacancies and the crystal chemistry of breakdown reactions in kimberlitic omphacites. Am. Mineral. 65, 1185–1191.

Stixrude, L., Lithgow-Bertelloni, C., (2012) Geophysics of chemical heterogeneity in the mantle. Ann. Rev. Earth Planet. Sci. 40, 569-595.

Stöffler, D., Keil, K., Scott, E.R.D., 1991. Shock metamorphism of ordinary chondrites. Geochim. Cosmochim. Acta 55, 3845–3867.

Tutti, F., (2007) Formation of end-member $NaAlSi_3O_8$ hollandite-type structure (lingunite) in diamond anvil cell. Phys. Earth Planet. Sci. 161, 143-149.

Tutti, F., Dubrovinsky, L.S., Saxena, S.K., 2000. High pressure phase transformation of jadeite and stability of $NaAlSiO_4$ with calcium-ferrite type structure in the lower mantle conditions. Geophys. Res. Lett. 27, 2025-2028.

Udry, A., Balta, J.B., McSween, H.Y., 2013. CSD measurement on olivine grains in the Tissint meteorite. Lunar Planet. Sci. Conf. 44. 1266. pdf

Von Dreele, R.B., 1997. Quantitative texture analysis by Rietveld refinement**.** J. Appl. Cryst. 30, 517–525.

Walton, E.L., Sharp, T.G., Hu, J., Filiberto, J., 2014. Heterogeneous mineral assemblages in martian meteorite Tissint as a result of a recent small impact event on Mars. Geochim. Cosmochim. Acta 140, 334-348.

White, J.C., 1993. Shock-induced amorphous textures in plagioclase, Manicouagan, Quebec, Canada. Contrib. Mineral. Petrol. 113, 524-532.

Wood, B.J., Henderson, C.M.B., 1978. Compositions and unit-cell parameters of synthetic non-stoichiometric tschermakitic clinopyroxenes. Am. Mineral. 63, 66–72.

Wood, B.J., Holland, T.J.B., Newton, R.C., Kleppa, O.J., 1980. Thermochemistry of jadeite—diopside pyroxenes. Geochim. Cosmochim. Acta 44, 1363–1371.

Yagi, A., Suzuki, T., Akaogi, M., 1994. High pressure transitions in the system $KAlSi_3O_8$-$NaAlSi_3O_8$. Phys. Chem. Minerals 21, 12–17.

Yang, H., Konzett, J., Frost, D.J., Downs, R.T., 2009. X-ray diffraction and Raman spectroscopic study of clinopyroxenes with six-coordinated Si in the $Na(Mg_{0.5}Si_{0.5})Si_2O_6$-$NaAlSi_2O_6$ system. Am. Mineral. 94, 942–949.

Zhao, S., Nee, P., Green, H.W., Dobrzhinetskaya, L.F., 2011. Ca-Eskola component in clinopyroxene: Experiemntal studies at high pressures and high temperatures in multianvil apparatus. Earth Planet. Sci. Lett. 307, 517–524.

Table 1

Electron microprobe analytical results for wormy and rimming tissintite, and associated phases.

Oxide	Wormy type tissintite	Maskelynite associated with wormy tissintite	Rimming tissintite	Maskelynite associated with rimming tissintite	Maskelynite away from melt pockets	Pigeonite surrounding tissintite	Fayalite[d] surrounding tissintite
	n=6[a]	n=6	n=6	n=9	n=17	n=7	n=5
SiO_2	53.0(0.3)[b]	52.8(0.9)	53.2(0.3)	52.6(0.3)	53.7(0.9)	53.6(0.8)	35(1)
TiO_2	0.08(0.03)	0.07(0.04)	0.05(0.02)	0.04(0.02)	0.07(0.03)	0.09(0.04)	0.56(0.09)
Al_2O_3	29.2(0.3)	28.5(0.5)	29.7(0.2)	29.3(0.2)	29.1(0.6)	2.7(0.5)	3.3(0.5)
FeO	0.96(0.02)	1.3(0.4)	0.85(0.06)	0.79(0.07)	0.7(0.1)	13.3(0.7)	40(1)
MgO	0.18(0.02)	0.3(0.3)	0.17(0.02)	0.17(0.04)	0.15(0.06)	22.6(0.6)	15(1)
CaO	12.5(0.2)	12.4(0.1)	13.0(0.2)	12.9(0.1)	12.5(0.7)	6.1(0.5)	4.7(0.5)
Na_2O	4.7(0.2)	3.53(0.08)	3.9(0.1)	3.5(0.1)	3.9(0.3)	0.4(0.1)	0.39(0.05)
K_2O	0.06(0.01)	0.08(0.03)	0.06(0.01)	0.10(0.03)	0.1(0.1)	b.d.	0.06(0.03)
Cr_2O_3	b.d.[c]	b.d.	b.d.	b.d.	b.d.	0.52(0.08)	0.56(0.06)
MnO	b.d.	b.d.	b.d.	b.d.	b.d.	0.46(0.07)	0.85(0.03)
Total	100.7	99.0	100.9	99.4	100.2	99.8	100
Ca/(Ca+Na+K) atomic ratio as %	59	66	65	67	63		
No. O atoms	6	8	6	8	8	6	4
Si	1.80	2.42	1.80	2.40	2.43	1.95	1.01
Ti	0.00	0.00	0.00	0.00	0.00	0.00	0.01
Al	1.17	1.54	1.18	1.58	1.55	0.12	0.11
Fe	0.03	0.05	0.02	0.03	0.03	0.41	0.96
Mg	0.01	0.02	0.01	0.01	0.01	1.23	0.64
Ca	0.45	0.61	0.47	0.63	0.61	0.24	0.14
Na	0.31	0.31	0.26	0.31	0.34	0.03	0.02
K	0.00	0.00	0.00	0.01	0.01		0.00
Cr						0.01	0.01
Mn						0.01	0.02
Sum cations	3.77	4.95	3.74	4.97	4.98	4.00	2.92

[a]n = number of analyses.
[b]Errors given inside parentheses are one standard deviation of the mean based on all of the analyses.
[c]b.d.= below detection limit: 0.02 wt% K, 0.05 wt% Cr, 0.06 wt% Mn.
[d]Slightly contaminated by co-existing pigeonite.

Table 2
Observed reflections of tissintite.

h	*k*	*l*	d (Å)
-3	3	3	1.49261
-2	2	2	2.13817
-2	6	0	1.41584
-2	8	2	1.04032
-1	-1	3	1.69708
-1	1	2	2.56655
-1	3	0	2.92434
-1	5	-1	1.67728
-1	5	1	1.69769
-1	7	0	1.27315
0	-2	2	2.13957
0	4	-2	1.67252
1	-3	0	2.88943
2	-6	0	1.44849
2	-6	3	1.01711
2	-4	-2	1.67187
2	-4	1	1.76702
2	-2	-2	2.22146
2	-2	-1	2.99316
3	-5	-1	1.53530
3	-5	1	1.38139
3	-1	-3	1.65521
4	-2	-3	1.49224
4	0	-5	1.02196

Table 3
Symmetry Modes for group - subgroup pair $P\bar{3}1c \rightarrow C2/c$. The index of this group-subgroup pair is 3 and the transformation matrix is b, -2a-b, c (read by columns).

Table 3a: Symmetry Modes Summary (primary condensing modes in bold)

WP	Modes
12i	$\Gamma_1^+(3)$ $\mathbf{\Gamma_3^+(6)}$
6h	$\Gamma_1^+(1)$ $\mathbf{\Gamma_3^+(3)}$
2c	$\mathbf{\Gamma_3^+(1)}$
2a	$\mathbf{\Gamma_3^+(1)}$

Table 3b: Splitting of Wyckoff positions

No	Wyckoff position(s)	
	Group	Subgroup
1	12i	8f 8f 8f
2	6h	8f 4e
3	2c	4e
4	2a	4e

(a)

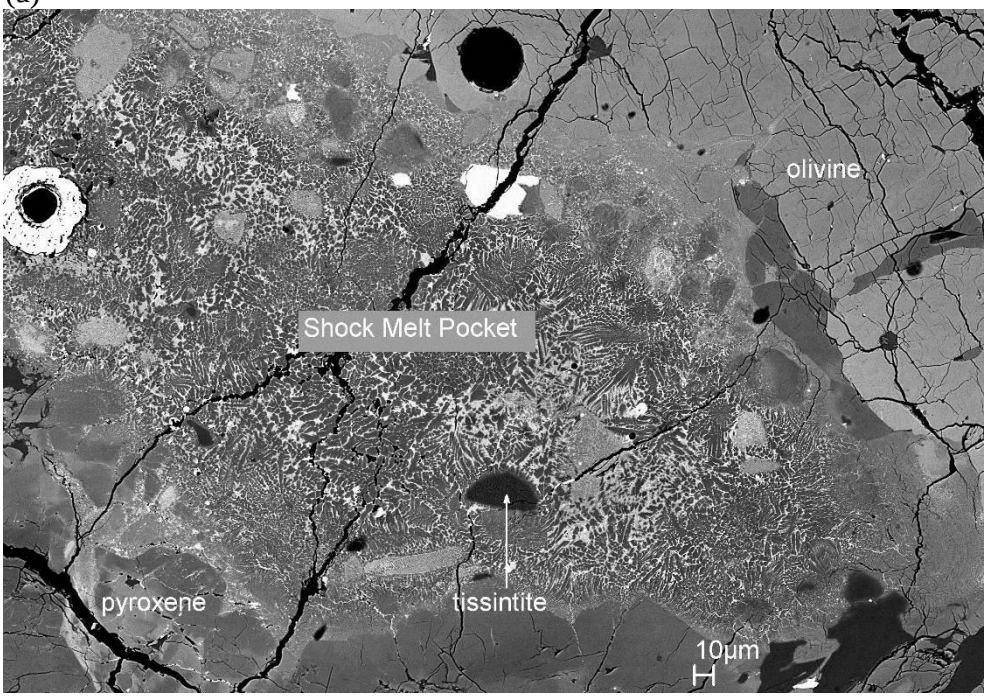
olivine
Shock Melt Pocket
pyroxene
tissintite
10μm

(b)

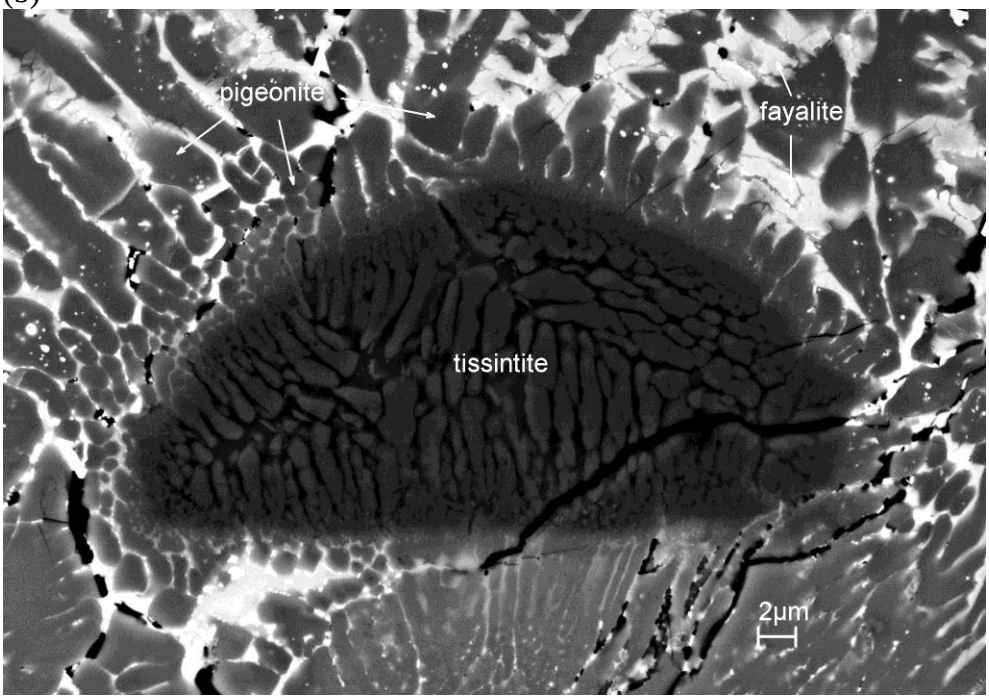
pigeonite
fayalite
tissintite
2μm

(c)

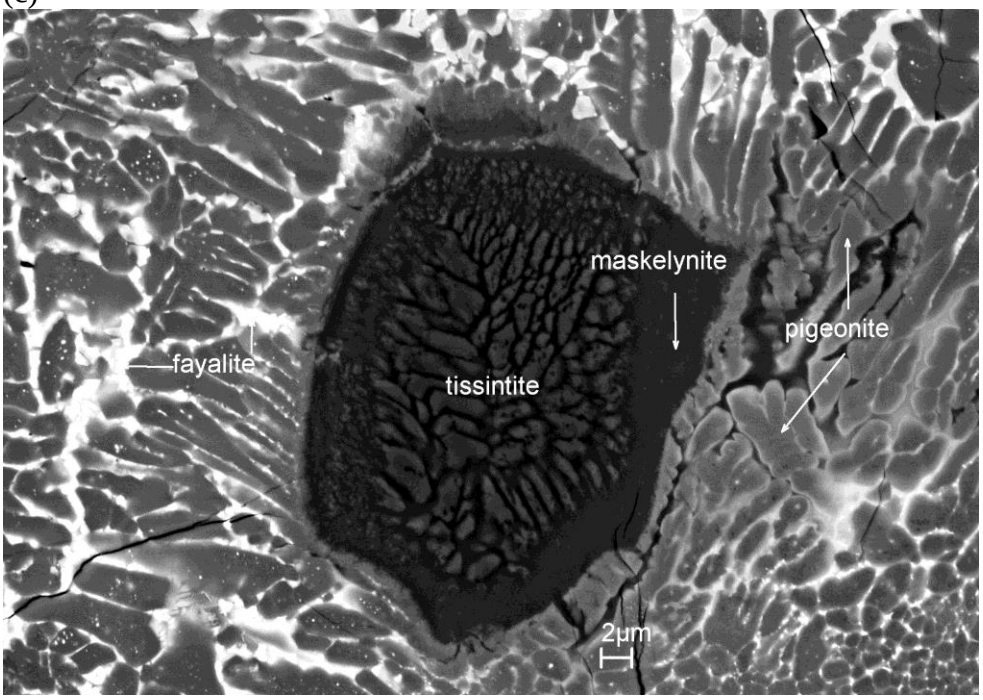

(d)

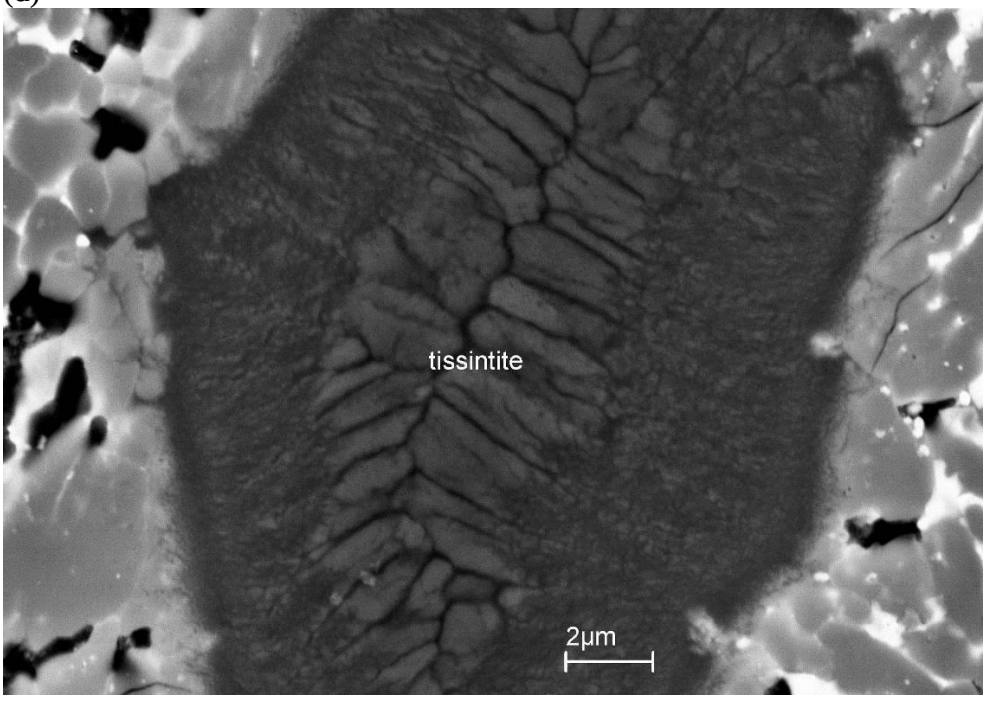

Fig. 1. (a) SEM BSE image showing tissintite in a shock melt pocket, in Tissint section UT2. (b) Enlarged BSE image revealing fine-grained tissintite with surrounding diopside and fayalite. (c-d) SEM BSE images of additional tissintite occurrences from UT1.

(a)

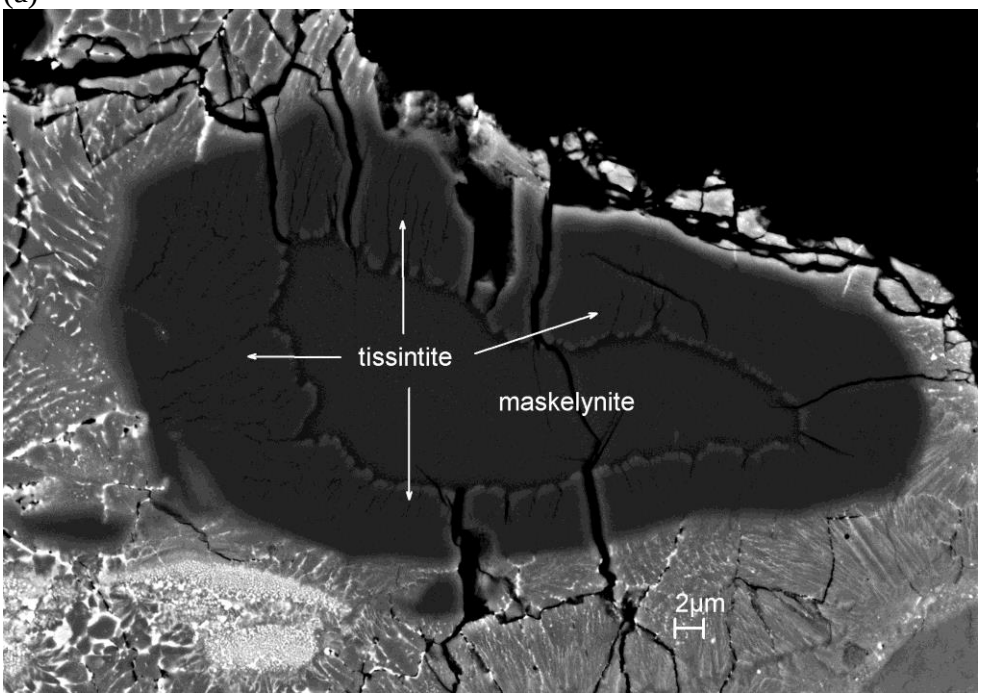

(b)

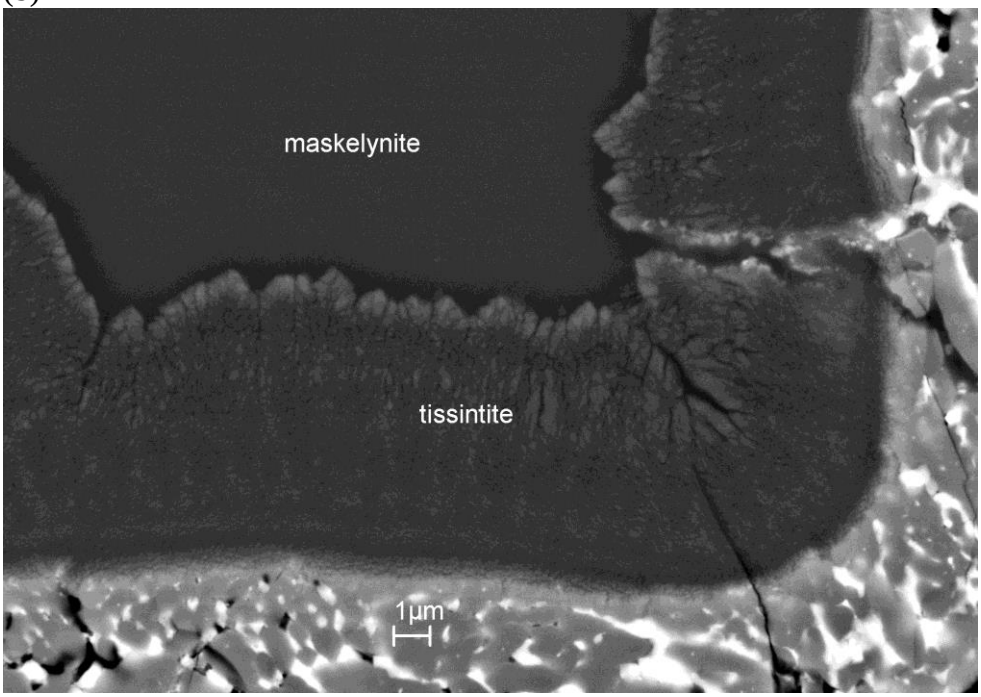

(c)

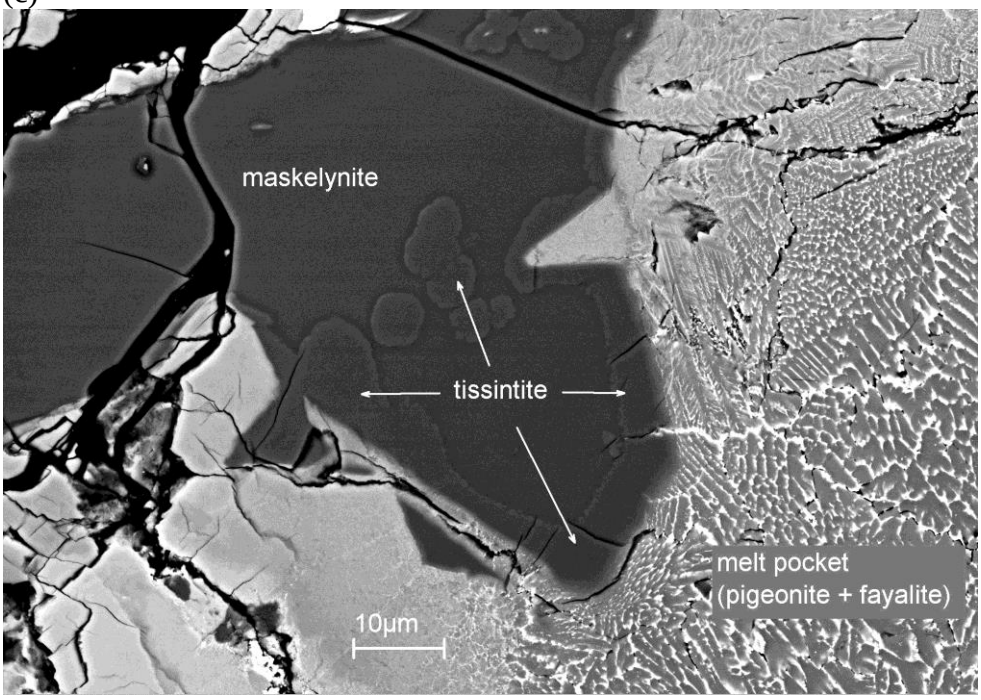

Fig. 2. SEM BSE images showing tissintite crystals in Tissint section UT1. (a) Tissintite forms a rim that completely surrounds plagioclase glass in the interior and thereby separates it from the host melt pocket. (b) A close-up of a rim region from a different tissintite occurrence in UT1, showing individual crystals. The crystal size is generally in the range of 100-500nm; crystals elsewhere in the meteorite can be as long as ~4 μm. (c) Tissintite crystals rim a large maskelynite where it came into contact with an adjacent melt pocket. The tissintite rim extends ~25 μm away from portions of the maskelynite that was in direct with the quench mat of the melt pocket in the plane of the section. The maskelynite containing the tissintite extends ~150 μm away from the melt pocket, but only within the closest ~25 μm does tissintite occur. Ringwoodite and the new mineral ahrensite occur on the opposite side of this melt pocket, ~150 μm away from the tissintite.

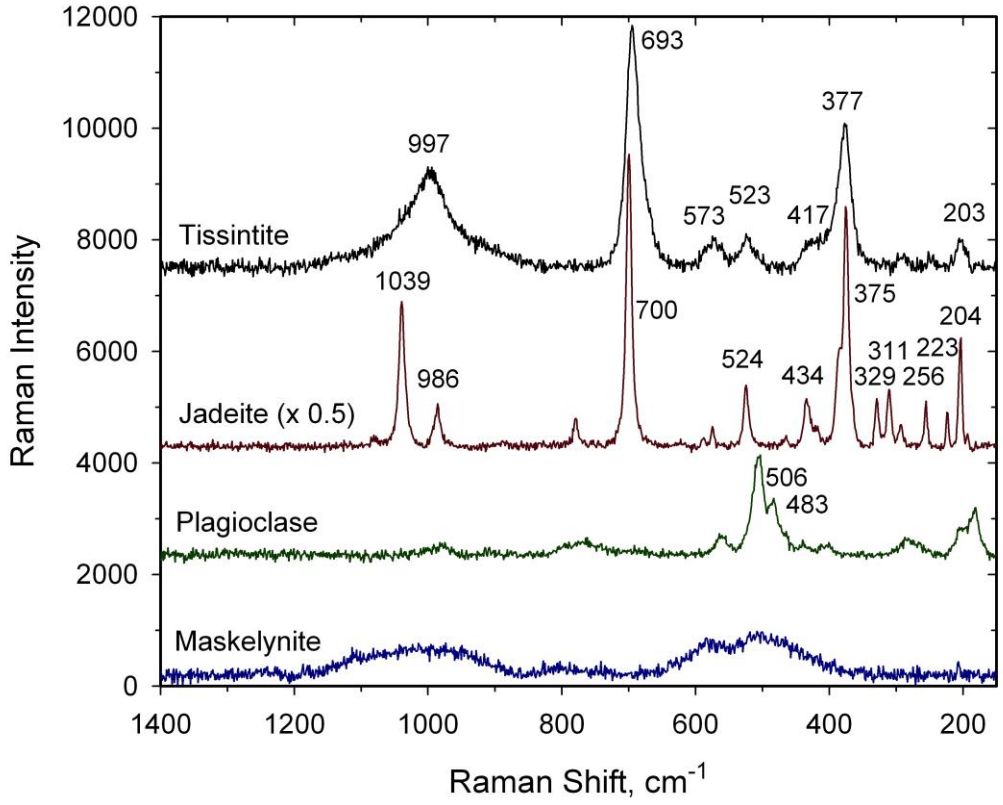

Fig. 3. Raman spectra of tissintite shown in Fig. 1b, maskelynite in Tissint (UT2), jadeite from a polished slab of colorless, polycrystalline Burmese jadeite, and plagioclase (An69.4) from the Ponderosa Mine, Harney Co., Oregon, USA (Johnston et al., 1991).

(a)

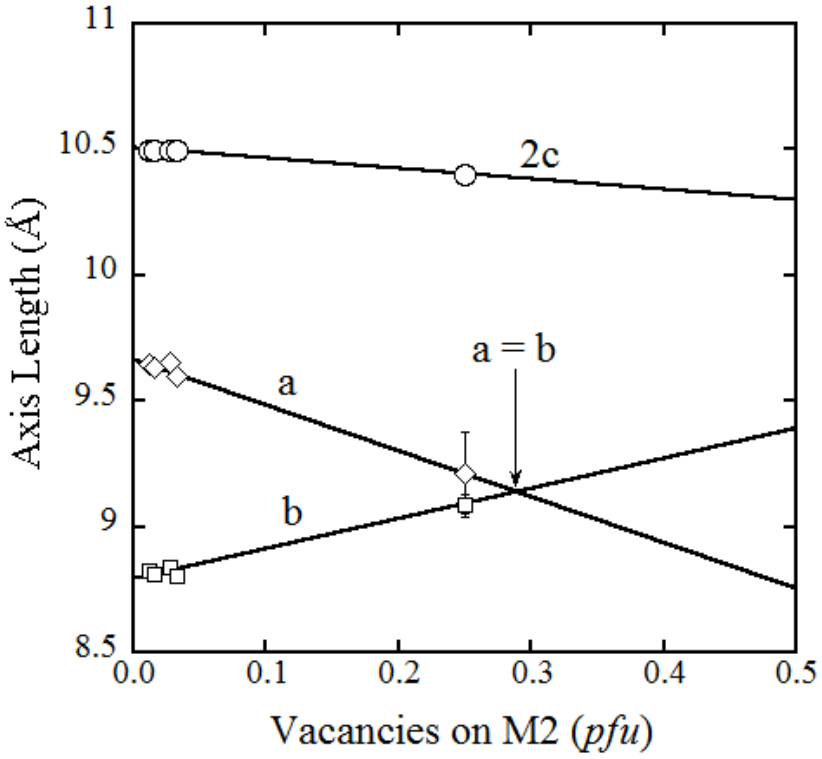
11
10.5
10
9.5
9
8.5
Axis Length (Å)
2c
a = b
a
b
0.0
0.1
0.2
0.3
0.4
0.5
Vacancies on M2 (*pfu*)

(b)

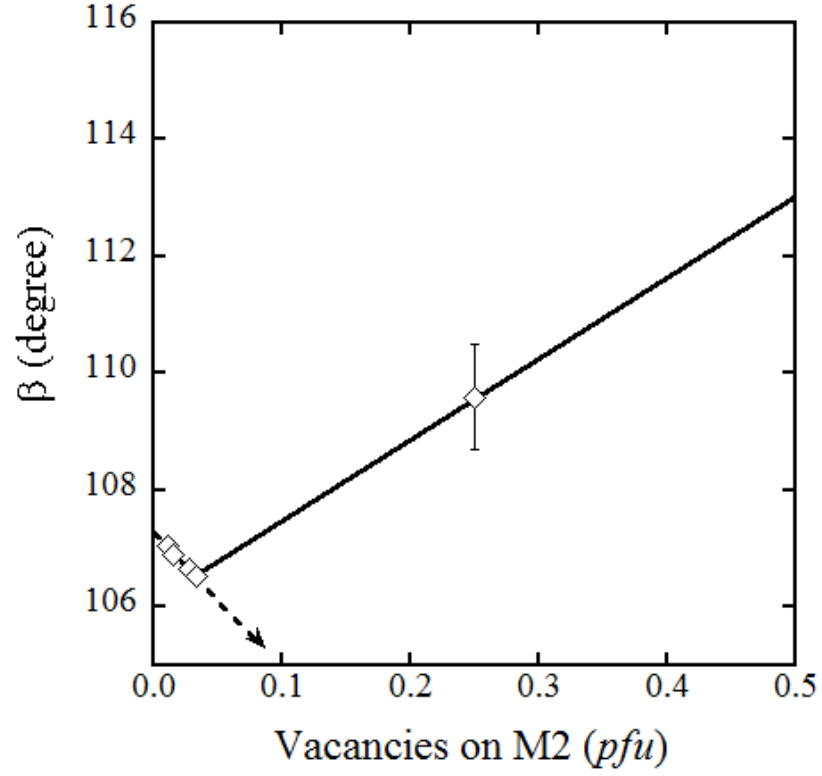
116
114
112
110
108
106
β (degree)
0.0
0.1
0.2
0.3
0.4
0.5
Vacancies on M2 (*pfu*)

(c)

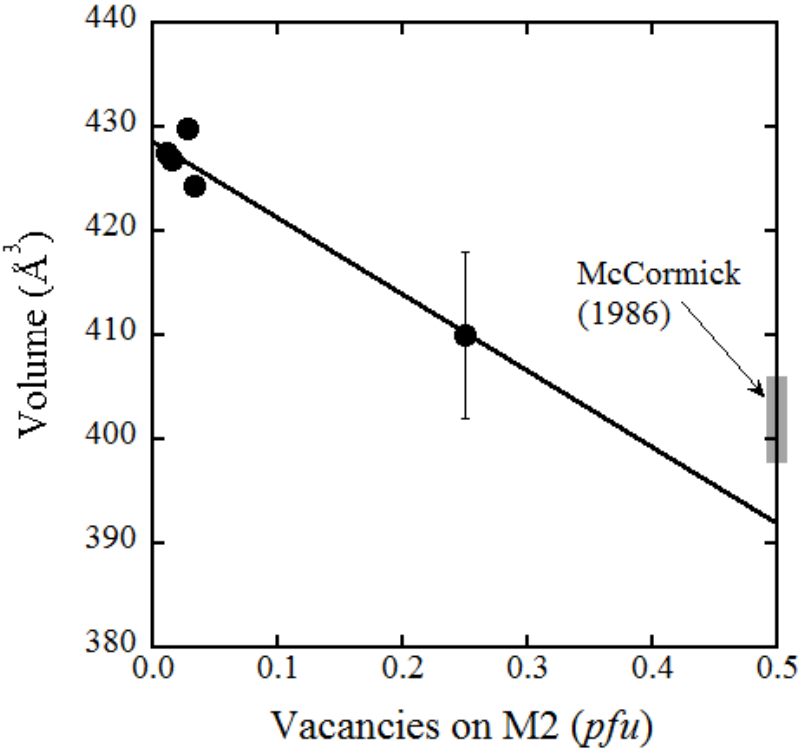
440
430
420
410
400
390
380
Volume (Å^3)
0.0
0.1
0.2
0.3
0.4
0.5
Vacancies on M2 (*pfu*)
McCormick
(1986)

(d)

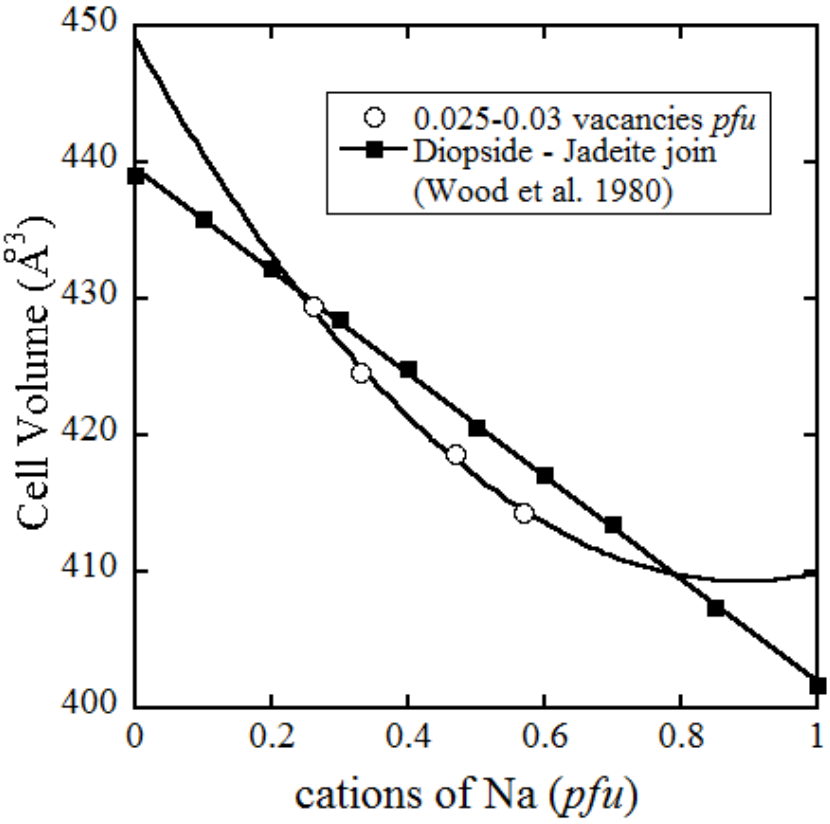
450
440
430
420
410
400
Cell Volume (Å^3)
0
0.2
0.4
0.6
0.8
1
cations of Na (*pfu*)
0.025-0.03 vacancies *pfu*
Diopside - Jadeite join
(Wood et al. 1980)

Fig. 4. Cell parameters for type tissintite (Ca# = 59) and *C2/c* clinopyroxenes from the literature with Ca# of 54-64. The literature data are taken from McCormick (1986), Oberti and Caporuscio (1991), and Nestola et al. (2007) where the vacancy concentration was determined by structure analysis. Lines are unweighted regressions. (a) Cell parameters a, b, and 2 times c (for visual clarity) as a function of vacancy concentration. (b) Unique angle β as a function of vacancy concentration. (c) Cell volume as a function of vacancy concentration. The dashed lines are unweighted regression through the data and pertain to a Ca# of 54-64. In Fig. 3a, the vacancy concentration where a- and b- axes assume equal value is indicated. This may mark the point at which a spontaneous elastic instability of the defective pyroxene structure is induced. (d) Cell volume as a function of Na for clinopyroxenes with 0.025 – 0.30 vacancies *pfu*. Also shown are cell volumes for clinopyroxenes along the jadeite – diopside join (Wood et al. 1980).

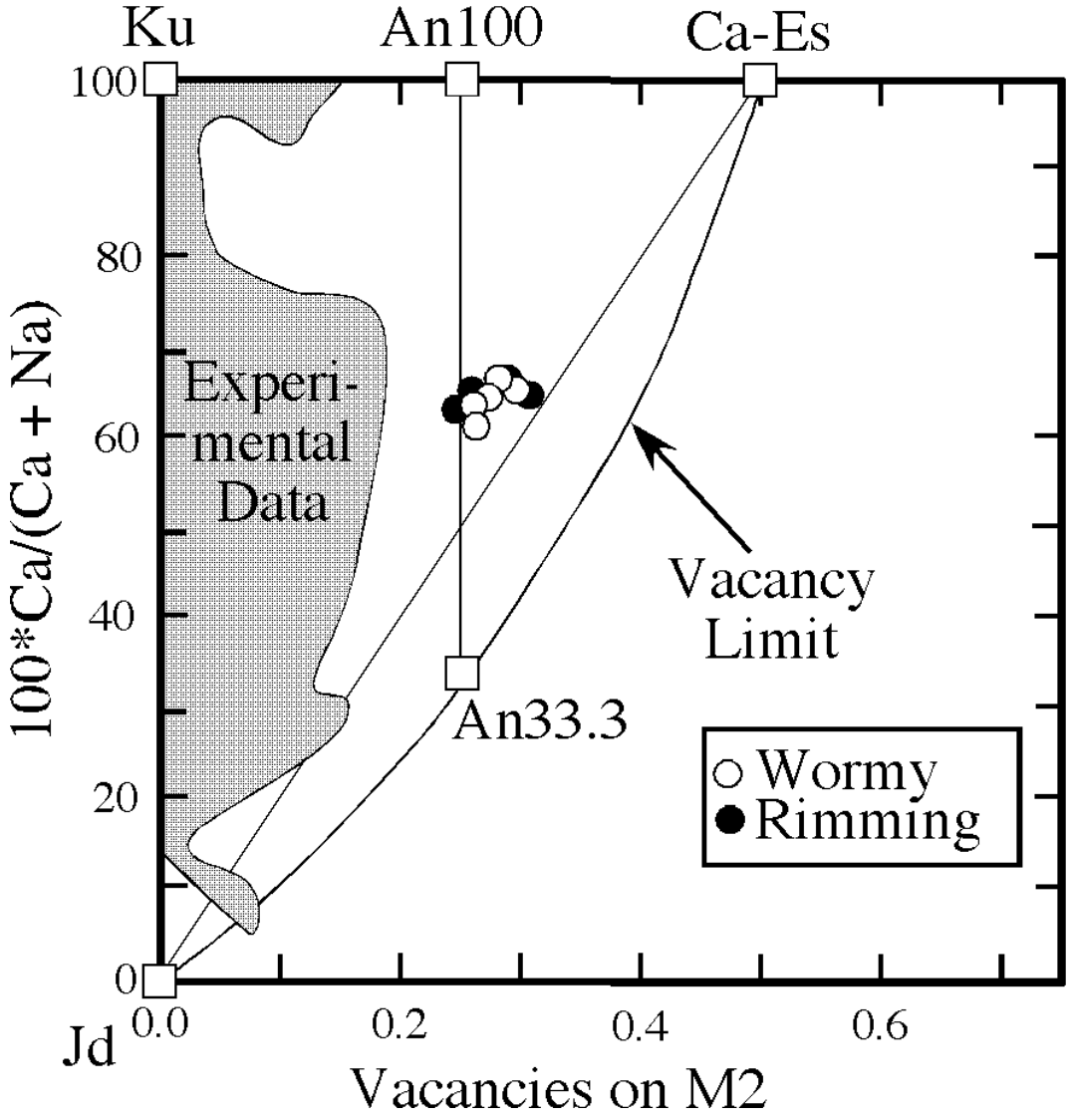

Fig. 5. Ca #, molar Ca/(Ca+Na), expressed as percent, in tissinitite, as a function of the concentration of vacancies on the M2 site sorted by textural occurrence. Compositions of clinopyroxenes are restricted to the portion of the diagram above the curve labeled "Vacancy Limit," which defines the locus of points for which the M1 site is fully occupied with 3+ cations and the tetrahedral site by 4+ cations. Compositions for Ca-Na plagioclase defined in terms of a clinopyroxene formula unit, plot along a vertical line at an M2 vacancy concentration of 0.25; this line extends from end-member anorthite (Ca# of 100), labeled An100, to a Ca# of 33.3, below which clinopyroxene formulas based on M2 vacancies cannot be constructed from plagioclase. Compositions for jadeite (Jd), kushiroite (Ku), and the Ca-Eskola component (Ca-Es) are also shown. The gray field encloses data from equilibration and synthesis experiments of Wood and Henderson (1978), Gasparik (1984, 1985, 1986), Irifune et al. (1986), Ono and Yasuda (1996), Pertermann and Hirschmann (2002), Okamoto and Maruyama (2004), Zhao et al. (2011), Ishii et al. (2012), Massone and Fockenberg (2012), and Knapp et al. (2013).

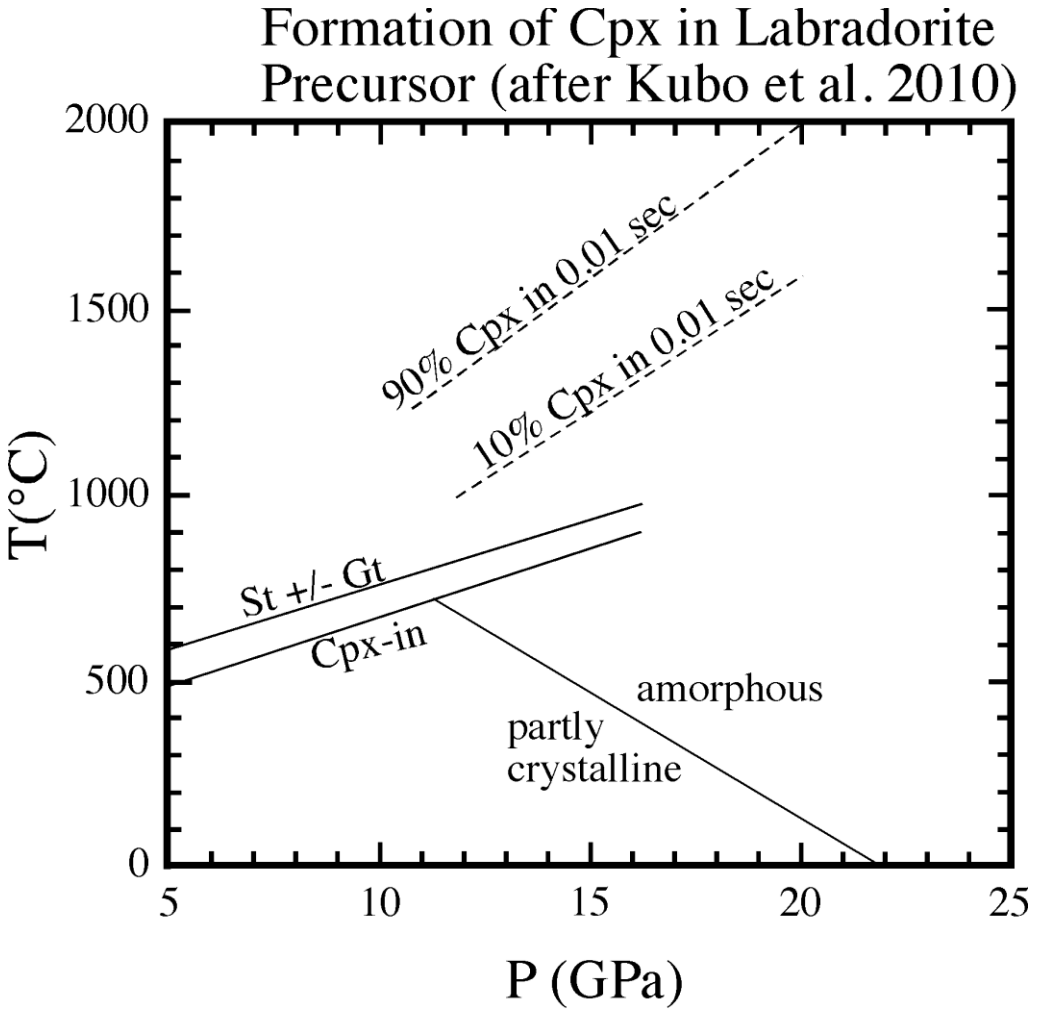

Fig. 6. Evolution of plagioclase (An58) during rapid heating and pressurization, modified after and combining elements of two figures in Kubo et al. (2010). The solid lines refer to experiments in which powdered natural labradorite was cold pressed and then heated (rate not stated). Amorphization versus X-ray diffraction occurs rapidly, within a second. If heated sufficiently, clinopyroxene (Cpx) nucleates and grows but with further heating, stishovite (St) ± garnet (Gt) grow and replace the clinopyroxene. Dashed lines are calculated amounts of clinopyroxene crystallized in 0.01 seconds after an instantaneous elevation of pressure and temperature, from ambient (e.g., after a shock event). Although presented quantitatively, this figure is best thought of as schematic. Fig. 6 is not a phase diagram and the appearance temperatures for clinopyroxene indicated on the figure are a measure of time at P and T, not a representation of stable phase fields. Kubo et al. (2010) determined volume fractions of clinopyroxene at constant pressure and temperature as a function of time; fit their data to an Avrami equation; and extrapolated the resulting kinetic parameters to the short-time scales of a shock event in order to calculate degrees of conversion of amorphous plagioclase composition material into clinopyroxene. Even on a very-short time scale, considerable crystallization of clinopyroxene is possible at relatively low temperatures (dashed lines in Fig. 6).